Nano Research

Open Access

Research Article

Constructing efficient ion transport channels via the "highway effect": Rational optimization of PVDF-based solid-state electrolytes through organic–inorganic composite doping

Liubin Song[1], Yiyu Xiong[1], Xingli Xiao[2], Zhongliang Xiao[2], Tianyuan Long[2], Daoxin Wu[1], Yinjie Kuang[1], Xue Wen[3], Tingting Zhao[1] ✉, and Fulu Chu[4] ✉

[1] School of Chemistry and Pharmaceutical Engineering, Changsha University of Science and Technology, Changsha 410114, China
[2] Hunan Happy Times New Energy Co., Ltd., Shaoyang 422000, China
[3] College of Mechanical and Energy Engineering, Shaoyang University, Shaoyang 422099, China
[4] School of Materials Science and Engineering, University of Jinan, Jinan 250022, China

Cite this article: *Nano Research*, **2026**, *19*, 94908656. https://doi.org/10.26599/NR.2026.94908656

ABSTRACT: Polyvinylidene fluoride (PVDF)-based solid polymer electrolytes (SPEs) show great potential for solid-state lithium metal batteries (SSLMBs) due to their high ionic conductivity, wide electrochemical window, and cost-effectiveness. However, they suffer from low room-temperature ionic conductivity and poor electrode–electrolyte interfacial compatibility, limiting their practical application. Herein, an organic–inorganic synergistic modification strategy is proposed that hexadecyltrimethoxysilane (HDTMS)-modified nano-silica (Mod-SiO_2) is incorporated into a PVDF/polyacrylonitrile (PAN)/lithium salts blend to fabricate a composite solid electrolyte (PVDF/PAN/lithium salt/Mod-SiO_2 (PPLS) composite system). Specifically, PAN facilitates PVDF molecular chains' motion to enhance segmental mobility, while uniformly dispersed Mod-SiO_2 constructs continuous three-dimensional (3D) Li^+ transport channels. This synergistic "ion-transport highway" effect boosts Li^+ mobility and optimizes dispersion uniformity, ionic conductivity, and interfacial stability. At room temperature, the PPLS exhibits an ionic conductivity of 4.83 × 10^{-4} S·cm^{-1}, a Li^+ transference number of 0.7, and an extended electrochemical window of 5.1 V. $LiFePO_4$|PPLS|Li batteries retain 80.9% capacity retention after 1000 cycles, with a Coulombic efficiency of 99.3%. This work provides valuable insights for the rational design and optimization of PVDF-based SPEs and advances the practical development of high-safety SSLMBs.

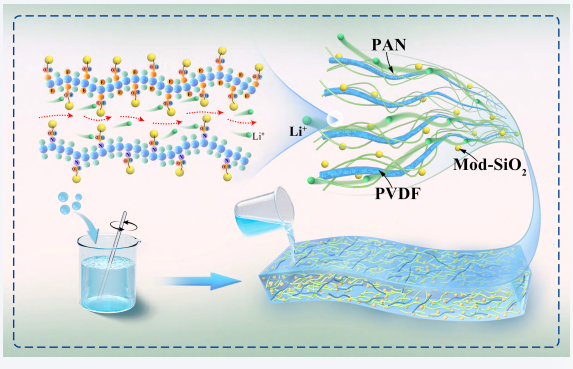

KEYWORDS: polyvinylidene fluoride, composite solid-state electrolyte, three-dimensional ion transport channel, modified nano-silica (Mod-SiO_2)

1 Introduction

Regarded as a premier future battery technology, solid-state lithium metal batteries (SSLMBs) offer a combination of outstanding safety, high theoretical capacity, robust mechanical strength, and remarkable electrochemical stability [1–3]. At present, solid-state electrolytes can be primarily categorized into inorganic solid-state electrolytes (ISEs) and organic solid polymer electrolytes (SPEs). Despite typically exhibiting high ionic conductivity (~ 10^{-3} S·cm^{-1}) [4, 5], ISEs suffer from inadequate interfacial contact with the electrodes [6]. This limitation has driven considerable attention toward SPEs, which benefit from excellent flexibility and superior interfacial contact.

In recent years, polyvinylidene fluoride (PVDF) has been widely utilized as a polymeric solid-state electrolyte material due to its high dielectric constant. PVDF-based polymer electrolytes demonstrate moderate ionic conductivity at room temperature (10^{-5}–10^{-6} S·cm^{-1}) [7], along with a wide electrochemical stability window (4.5 V) [8] and excellent thermal stability, making them among the most promising candidates for solid-state electrolyte applications [9]. However, PVDF suffers from poor interfacial contact with

Received: January 23, 2026; **Revised:** March 2, 2026
Accepted: March 20, 2026

✉Address correspondence to Tingting Zhao, zhaott_468@163.com; Fulu Chu, mse_chufl@ujn.edu.cn

electrodes, which increases internal cell resistance. This not only deteriorates rate capability but also impedes interfacial charge transfer and promotes non-uniform lithium deposition. As a result, lithium dendrite growth is exacerbated, and interfacial side reactions are intensified under high-voltage conditions, ultimately undermining the electrochemical stability of the battery system [10–13].

To mitigate these limitations, extensive research has incorporated polyacrylonitrile (PAN) into polymer electrolyte matrices. The nitrile group (C≡N) in PAN can form strong Lewis acid-base interactions with both Li^+ cations and anions from lithium salts, thereby significantly improving ionic dissociation efficiency and enhancing ionic conductivity [14–16]. Moreover, PAN exhibits a high oxidation decomposition potential, enabling compatibility with high-voltage cathode materials and compensating for the insufficient interfacial stability of PVDF under elevated voltages. Consequently, the blending of PVDF and PAN has been extensively explored, as this strategy enhances electrode/electrolyte interfacial compatibility by modulating polymer segment polarity, thus improving battery rate performance [17–20]. Nevertheless, the inherent porous morphology of polymer electrolytes may disrupt continuous ion transport pathways, leading to uneven lithium plating and accelerated dendrite propagation [21–23]. Therefore, satisfying the multifaceted requirements of fast-charging solid-state lithium metal batteries for practical deployment remains a significant challenge [24–26].

To achieve uniform lithium deposition, optimize the interfacial environment, and enhance lithium-ion transport kinetics, organic–inorganic composite solid-state electrolytes have become a focal point of research [27–29]. The incorporation of inorganic fillers establishes continuous ionic conduction pathways while effectively regulating lithium nucleation sites and growth orientation, thereby suppressing dendrite formation [30–32]. Moreover, fillers enhance interfacial wettability between the polymer matrix and electrodes, leading to reduced interfacial impedance [33–35]. For example, Liu et al. [36] employed negatively charged group-functionalized aramid nanofibers (Kevlar (poly(*p*-phenylene terephthalate)) nanofibers (KANFs)) as a rigid scaffold, integrated with metal–organic framework (MOF) bridging and deep eutectic solvent (DES) modification, to fabricate a highly rigid and stable composite electrolyte system. Similarly, Wang et al. [37] developed an ultrathin polymer/$Li_{6.4}La_3Zr_{1.4}Ta_{0.6}O_{12}$ (LLZTO) composite electrolyte film (LPCE) that enables rapid lithium-ion conduction and promotes the formation of a robust solid electrolyte interphase (SEI) layer at the lithium–metal interface, thereby significantly improving battery cycling stability. These composite electrolytes exhibit significant advantages in enhancing ionic conductivity, improving mechanical strength, inhibiting lithium dendrite propagation, and stabilizing the electrode/electrolyte interface [38]. However, non-uniform dispersion of fillers within the polymer matrix often results in agglomeration, which disrupts ion transport pathways and limits the full utilization of filler functionality. Therefore, effectively addressing the challenge of homogeneous filler distribution is not only critical for optimizing the performance of composite electrolytes but also constitutes a key enabler for their scalable industrial application.

To address this issue, this work employed organic blending of PAN with PVDF to enhance electrode–electrolyte interfacial compatibility. Concurrently, the incorporation of hexadecyltrimethoxysilane (HDTMS)-surface-modified nano-silica (Mod-SiO_2) optimizes the interface and improves filler dispersion uniformity, thereby synergistically enhancing the overall performance of the solid electrolyte. The as-synthesized PVDF/PAN/lithium salt/Mod-SiO_2 (PPLS) composite system electrolyte exhibits outstanding electrochemical performance, with ionic conductivity reaching 4.83×10^{-4} S·cm^{-1}, lithium ion migration number peaks at 0.70, and the electrochemical window extends to 5.1 V. Li||Li symmetric cells with PPLS sustain stability over 1400 charge–discharge cycles. Moreover, $LiFePO_4$|PPLS|Li cells maintain a capacity retention of 80.9% with a high Coulombic efficiency (CE) of 99.3% after 1000 cycles at room temperature, demonstrating remarkable cycling stability and practical utility.

2 Results and discussion

In this work, the long-chain alkyl groups in HDTMS molecules effectively hindered interparticle hydrogen bonding among SiO_2 nanoparticles via steric hindrance effects, thereby suppressing the undesired agglomeration of nanoparticles while notably enhancing their dispersibility in organic matrices. The Mod-SiO_2 can efficiently anchor the bis(trifluoromethanesulfonyl)imide ($TFSI^-$) anions in the lithium salt, increasing the free Li^+ concentration in the system, simultaneously enhancing ionic conductivity and electrochemical stability (Fig. 1(a)). The scanning electron microscopy (SEM) image in Fig. 1(b) shows that the particle size of Mod-SiO_2 is around 100 nm. The particles exhibit uniform size distribution with no surface impurities. The polyacrylonitrile–polypropylene (PPLS) composite solid electrolyte membrane (Figs. 1(c) and 1(d)) exhibits a dense, smooth surface with uniform elemental distribution. In contrast, the PVDF/PAN/lithium salt composite system (PPL) and PVDF /lithium salt composite system (PL) membranes display relatively rough surfaces (Figs. S1 and S2 in the Electronic Supplementary Material (ESM)). As shown in Fig. S3 in the ESM, Mod-SiO_2 is uniformly dispersed within the PPLS membrane, further demonstrating that HDTMS modification promotes homogeneous particle dispersion. The hydrophobic long chain of HDTMS is anchored onto the silica surface through chemical bonding, reducing surface energy and creating steric hindrance, thereby improving the interfacial compatibility with the polymer matrix. This effectively inhibits silica agglomeration and significantly enhances its dispersion stability in organic systems. Figure S4 in the ESM indicates that the tensile strength of PPLS-10 reaches 19.9 MPa, far exceeding the tensile strength of 2.3 MPa for PL solid-state electrolytes (PPLS-2.5 denotes the PPLS composite system containing 2.5% Mod-SiO_2, PPLS-5 denotes the PPLS composite system containing 5% Mod-SiO_2, and so on).

As shown in Fig. S5 in the ESM, the PL, PPL, and PPLS structures remain well-preserved, with peaks centered around 20°. Compared to PPL and PL, the peak of PPLS is weaker and more gradual, suggesting that PPLS has a lower crystallinity. The electrochemical impedance spectroscopy (EIS) demonstrated that the resistances of PPLS-2.5, PPLS-5, PPLS-10, and PPLS-15 were 43, 38.6, 31, and 38.6 Ω, respectively (Fig. 2(a)). In PPLS-2.5 and PPLS-5, a lower content of Mod-SiO_2 exerted no substantial impact on the dissociation of LiTFSI. Conversely, excessive Mod-SiO_2 content leads to agglomeration in PPLS-15, which was detrimental to the dissociation of LiTFSI. Consequently, PPLS-10 exhibited the highest ionic conductivity, reaching 4.83×10^{-4} S·cm^{-1}, which was significantly higher than that of PL (2.04×10^{-4} S·cm^{-1}) and PPL (4.08×10^{-4} S·cm^{-1}). The PPLS-10 electrolyte also shows the lowest

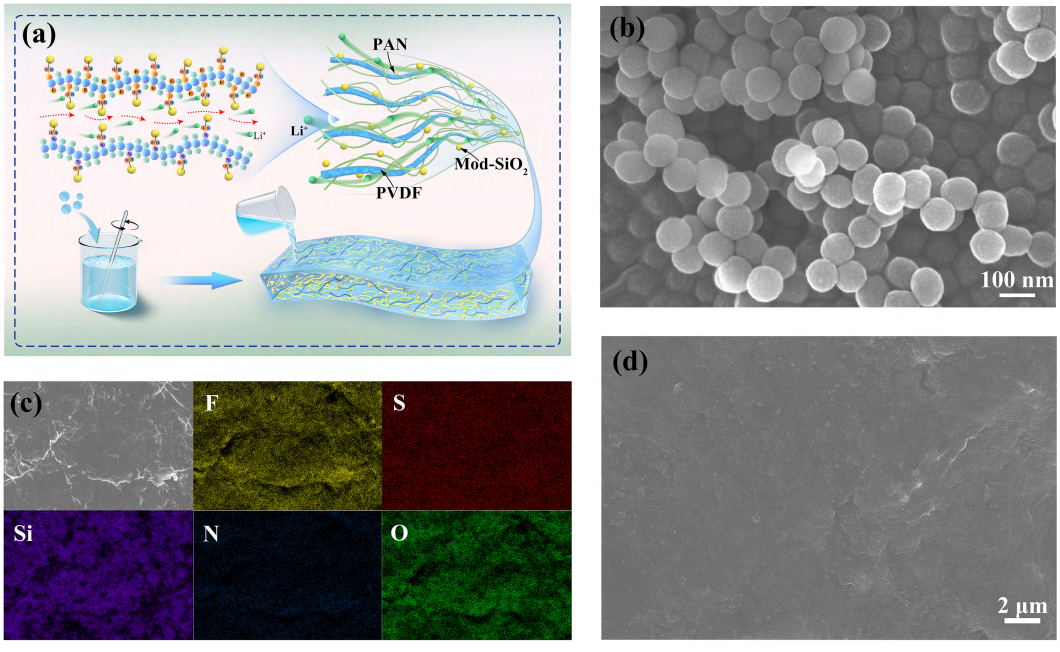

Figure 1 Ion conduction pathways and microstructural morphology of solid electrolytes. (a) Schematic illustration of the synthesis route and ion conduction mechanism of the PPLS solid electrolyte. (b) SEM image of Mod-SiO_2. (c) Energy-dispersive X-ray spectroscopy (EDS) elemental mapping (Si, F, N, S, and O) of the PPLS sample. (d) Surface morphology of the PPLS film observed via SEM.

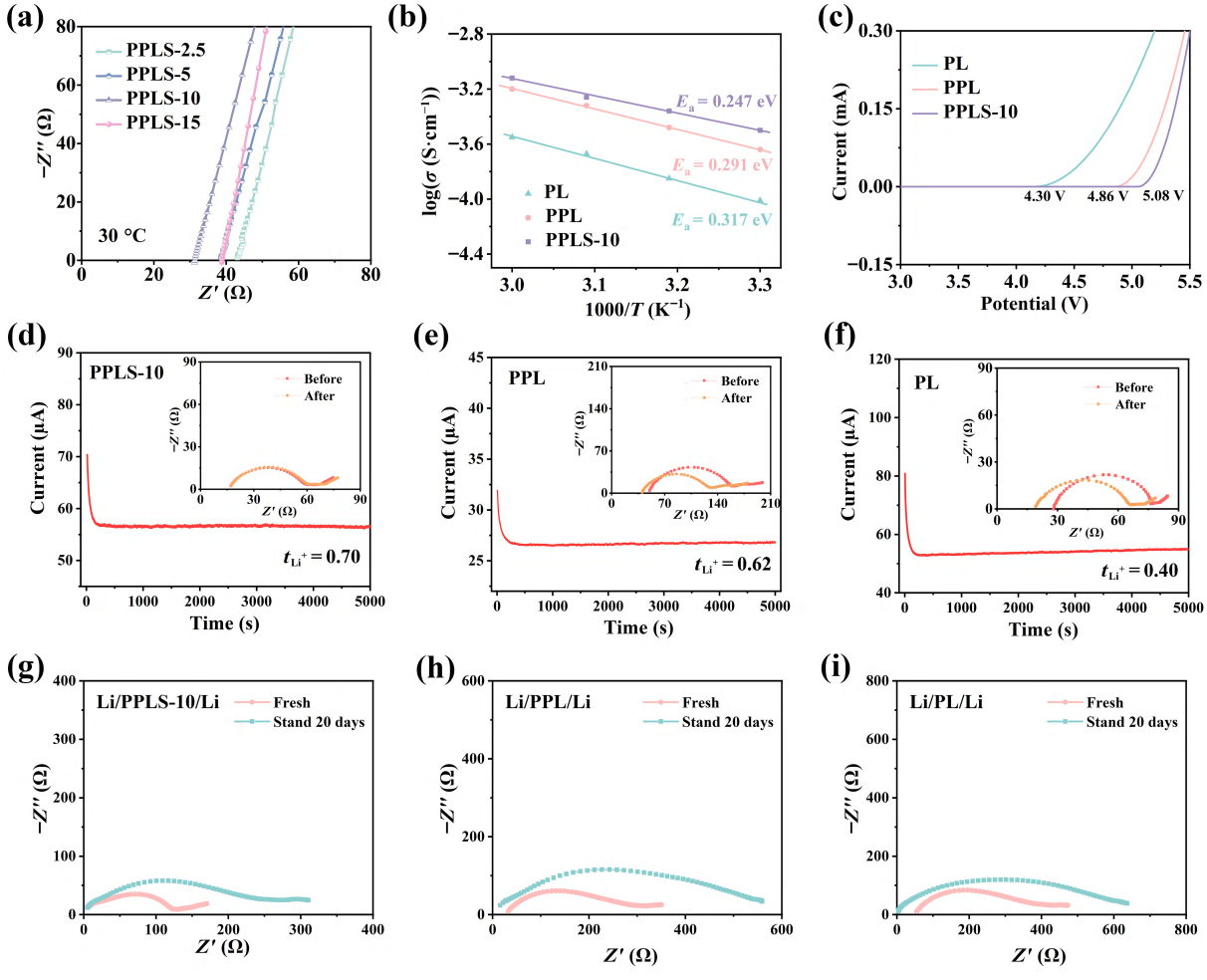

Figure 2 Electrochemical performance of solid electrolytes. (a) EIS comparison of PPLS-2.5, PPLS-5, PPLS-10, and PPLS-15 at 30 °C. (b) Arrhenius plots of the ionic conductivity vs. reciprocal temperature for PL, PPL, and PPLS-10. (c) LSV curves of PL, PPL, and PPLS-10. Polarization behavior and initial/steady-state EIS spectra of (d) PPLS-10, (e) PPL, and (f) PL. EIS comparison of the (g) Li/PPLS-10/Li, (h) Li/PPL/Li, and (i) Li/PPL/Li symmetric cells before and after 20 days of storage.

ion migration activation energy (E_a) of only 0.247 eV (Fig. 2(b)). The linear sweep voltammetry (LSV) curves presented in Fig. 2(c) indicated that, in comparison with PL and PPL, the oxidation stability window of PPLS-10 extended from 4.30 to 5.08 V. This finding suggested that the incorporation of PAN and Mod-SiO_2 could effectively anchor N-methyl-2-pyrrolidone (NMP), thereby expanding the oxidation potential of PPLS-10 and enabling it to be compatible with high-voltage cathodes. Furthermore, the lithium-ion transference numbers (t_{Li^+}) of PPLS-10, PPL, and PL were determined to be 0.70, 0.62, and 0.4, respectively (Figs. 2(d)–2(f)). These results indicated that the PAN enhances the migration rate of lithium ions, while the addition of Mod-SiO_2 provides interfacial migration pathways. The thermogravimetric analysis (TGA) measurements of PPLS-10 and PPL revealed that the contents of the NMP solvent were 21.17 wt.% and 12.9 wt.%, respectively (Fig. S6 in the ESM). The relatively high NMP content in PPLS-10 can be primarily attributed to the adsorption of NMP by Mod-SiO_2. The high residual solvent NMP adsorbed by SiO_2 is not only a physical adsorption phenomenon, but also acts as an *in-situ* plasticizer, which can reduce the crystallinity of PVDF, promote lithium salt dissociation, increase polymer chain mobility, and thus significantly improve ionic conductivity. Meanwhile, the solvent layer on the SiO_2 surface optimizes the interface contact and reduces interface impedance, which is beneficial to the electrochemical performance of solid electrolytes. The EIS results demonstrated that the charge-transfer resistance (R_{ct}) of the fresh Li/PPLS-10/Li symmetric cell (127.7 Ω) was substantially lower than that of the fresh Li/PPL/Li symmetric cell (319.5 Ω) and the Li/PL/Li symmetric cell (433.5 Ω) (Figs. 2(g)–2(i)). This finding indicates that the denser surface and fewer side reactions of PPLS-10 can significantly optimize the interfacial contact and stability with the lithium-metal anode. After 20 days of standing, the R_{ct} of the Li/PPLS-10/Li symmetric cell merely increased to 272.9 Ω, whereas the R_{ct} of the Li/PPL/Li symmetric cell escalated to over 500 Ω. This clearly shows that the introduction of Mod-SiO_2 effectively mitigates side reactions. The above-mentioned EIS results unambiguously indicate that even with a high NMP content, Mod-SiO_2 in PPLS-10 can firmly anchor the NMP solvent and inhibit interfacial reactions.

To clarify the chemical structure of the solid electrolyte membrane, the interactions between its components, and the dissociation behavior of lithium salts, we conducted the Fourier transform infrared (FTIR) and Raman spectroscopy on the solid electrolyte membrane. As depicted in Fig. 3(a), the FTIR results verify that the C=O and $-CH_3$ peaks of NMP at 1652.21 and 1405.37 cm^{-1} are shifted to 1663.79 and 1408.26 cm^{-1}, respectively. The blue shift of the C=O and $-CH_3$ peaks indicates a weakening of the hydrogen-bonding interaction between NMP molecules and Mod-SiO_2. This leads to a decrease in the polarity of NMP [39], thereby reducing the risk of side reactions between NMP and LiTFSI. Furthermore, this phenomenon suggests that the interaction between NMP and Mod-SiO_2 mainly involves physical encapsulation or spatial confinement rather than chemical bonding. Such an interaction is conducive to the homogeneous dispersion of nanoparticles, effectively preventing their agglomeration. Consequently, a dense and flexible electrolyte film can be formed,

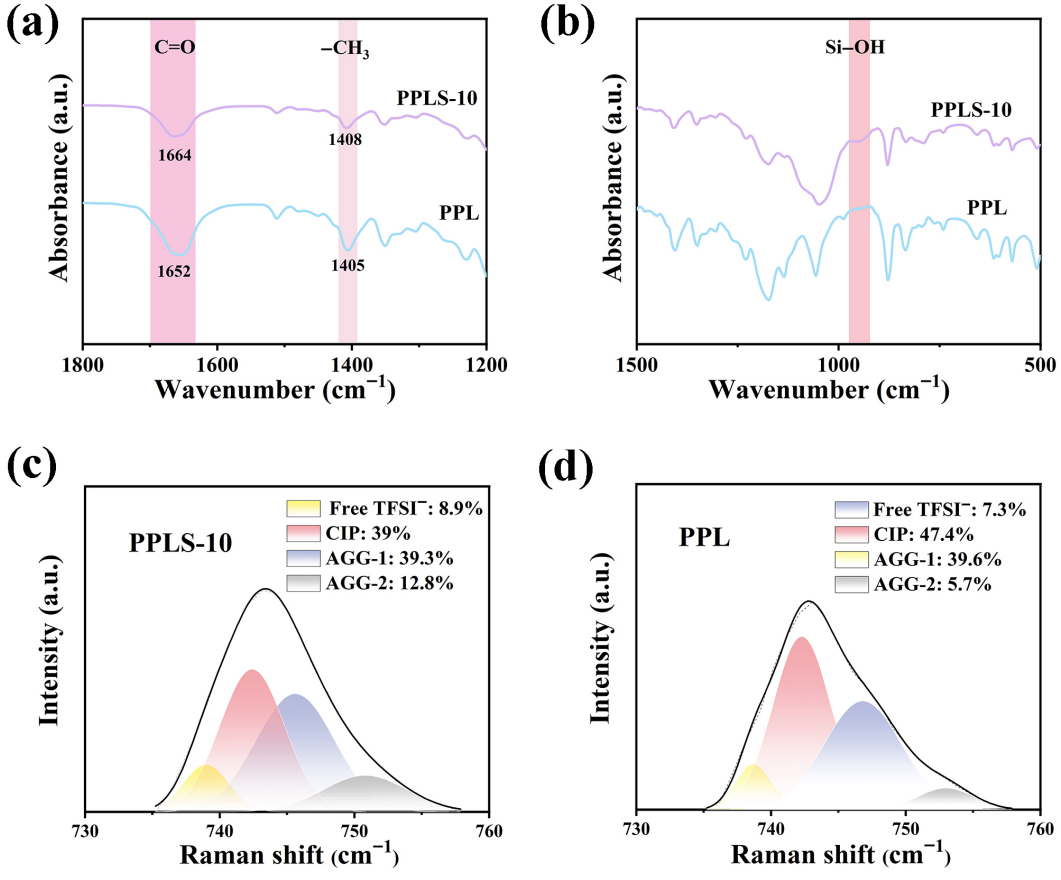

Figure 3 Chemical structure and functional group characterization of solid electrolytes: ((a) and (b)) FTIR spectra of PPL and PPLS-10. Raman spectra of (c) PPLS-10 and (d) PPL.

which helps to reduce the electrode–electrolyte interface impedance. The FTIR peaks at 950 cm^{-1} for PPLS-10, PPL, and PL clearly confirm the presence of Si–OH groups in the PPLS-10 electrolyte (Fig. 3(b)), indicating that Si–O bonds resonate with C–F, C–N, and C–H functional groups in PVDF and PAN segments, forming organic–inorganic interfacial channels. To reveal the role of PAN and Mod-SiO_2 on the dissociation behavior of LiTFSI in the electrolyte, we determined the coordination state of the $TFSI^-$ anion by Raman spectroscopy. In the PVDF electrolyte, the S–N–S band of $TFSI^-$ includes free $TFSI^-$ (738 cm^{-1}), contact ion pair (CIP, 743 cm^{-1}, one $TFSI^-$ combined with one Li^+), aggregated cluster AGG-1 (746 cm^{-1}, one Li^+ combined with two $TFSI^-$), and AGG-2 (752 cm^{-1}, one Li^+ combined with more than two $TFSI^-$) modes (Figs. 3(c) and 3(d) and Fig. S7 in the ESM). The content of free $TFSI^-$ in PPLS-10 is the highest, while that in PL is the lowest, indicating that the addition of PAN and Mod-SiO_2 can enhance the dissociation degree of lithium salt. The incorporation of PAN contributes to an increase in amorphous regions, expanding the lithium ion migration activity zone, enhancing segmental fluidity, and forming continuous lithium ion conduction pathways. Moreover, the Mod-SiO_2 with acidic Si–OH groups having an ultra-small size and good distribution, which can maximize the Lewis acid-base interaction with $TFSI^-$ anions, promoting the dissociation of LiTFSI and fixing $TFSI^-$ anions [40]. Meanwhile, with the addition of PAN and Mod-SiO_2, the proportion of CIP decreases from 56% to 39%, while the number of polymer clusters significantly increases. AGG-1 increases from 35.7% to 39.3%, and AGG-2 increases from 3.5% to 12.8%. This is conducive to the formation of an inorganic-rich SEI to enhance the interface stability. The above results verify that PAN and Mod-SiO_2 can effectively promote the dissociation of LiTFSI and fix $TFSI^-$ anions, thereby enabling PPLS-10 to achieve high ionic conductivity (4.83×10^{-4} $S \cdot cm^{-1}$) and Li^+ transference number (0.7).

To comprehensively characterize the electrochemical properties of PPLS-10, Li/PL/Li, Li/PPL/Li, and Li/PPLS-10/Li symmetric cells were assembled for in-depth testing. As depicted in Fig. 4(a), under a current density of 0.1 $mA \cdot cm^{-2}$, the Li/PPLS-10/Li symmetric cell demonstrated remarkable stability, capable of sustaining more than 1400 h of cycling. In contrast, the Li/PPL/Li symmetric cell could only maintain stable cycling for 800 h. Subsequent to 800 h of operation, the overpotential of the Li/PPL/Li symmetric cell experienced a sharp increase, rising from 40.8 to 127.3 mV. This phenomenon can be primarily attributed to the occurrence of severe side reactions at the interface between the electrolyte film and the lithium sheet. These side reactions led to a continuous elevation in the internal resistance, thereby disrupting the interfacial equilibrium. Even under a relatively higher current density of 0.2 $mA \cdot cm^{-2}$, the Li/PPLS-10/Li symmetric cell still achieved an impressively long cycle life of 400 h (Fig. S8 in the ESM). In addition, in the variable current cycling test, $LiFePO_4$/PPLS-10/Li was cycled at current densities of 0.05, 0.1, 0.2, and 0.5 $mA \cdot cm^{-2}$ for 200 h each, and then returned to a current density of 0.1 $mA \cdot cm^{-2}$ for stable cycling for more than 500 h. In contrast, Li/PL/Li and Li/PPL/Li experienced a rapid voltage rise to 5 V when the current density reached 0.5 $mA \cdot cm^{-2}$. This indicates that the addition of Mod-SiO_2 effectively improves the uniform deposition of lithium at high current, reduces the formation of lithium dendrites, maintains the stability of the solid electrolyte interface, and thus enables stable cycling (Fig. 4(b)). The long-cycle performance of the $LiFePO_4$/PPLS-10/Li solid-state battery exhibits a relatively high initial capacity. At a current rate of 1 C (1.0 C = 170 $mA \cdot g^{-1}$), the initial capacity reaches 168.9 $mAh \cdot g^{-1}$. After 1000 cycles, the capacity retention rate stands at 80.2%. For the $LiFePO_4$/PPL/Li solid-state battery, the capacity decay accelerates after 500 cycles. By the 1000-cycle mark, the capacity has decayed to zero. In contrast, the $LiFePO_4$/PL/Li solid-state battery demonstrates a significantly lower initial capacity, merely 131.3 $mAh \cdot g^{-1}$. Moreover, its capacity decays rapidly. Within less than 200 cycles, the capacity has decayed to an almost negligible level (Fig. 4(c)). Figure 4(d) depicts the rate performance of the full cells composed of PPLS-10, PPL, and PL. For the $LiFePO_4$/PPLS-10/Li solid-state battery, the discharge capacities at current rates of 0.1, 0.2, 0.5, 1, and 2 C are 165, 174, 173, 173, and 169 $mAh \cdot g^{-1}$, respectively. These values are notably higher than those of the $LiFePO_4$/PPL/Li and $LiFePO_4$/PL/Li cells (see Figs. S9–S11 in the ESM). The $LiFePO_4$/PPLS-10/Li solid-state battery also demonstrates excellent long-cycle performance at ambient temperature. As presented in Fig. 4(e), after 1000 cycles at a current rate of 0.2 C, it maintains a capacity retention rate of 80.9%. The PPLS-10 solid-state electrolyte is compatible with high-voltage cathodes and can be incorporated into full-cell configurations for charge–discharge cycling experiments. As illustrated, we fabricated an NCM811/PPLS-10/Li battery. This battery can stably undergo 100 cycles at a current rate of 0.5 C and room temperature, with a capacity retention rate reaching 83.3% (Fig. 4(f)). When compared with other reported works in the literature, it showcases significant advantages (Table S1 in the ESM).

Finally, to further elucidate the stability mechanism of PPLS-10, X-ray photoelectron spectroscopy (XPS) analysis was performed on the solid-state electrolytes within the Li/PL/Li, Li/PPL/Li, and Li/PPLS-10/Li symmetric cells following 100 h of cycling, as depicted in Fig. 5. In the C 1s spectra, the peaks corresponding to C–C, C–O, C=O, and C–F can be ascribed to the decomposition of NMP and PVDF. Regarding the F 1s spectra, the two characteristic peaks of inorganic LiF and organic C–F are positioned at 685.01 and 690.01 eV, respectively. The relative proportion of LiF detected in the solid–electrolyte interphase (SEI) formed by the PPLS-10 electrolyte (73.2%) is higher than the 63.8% and 68.9% observed for the PL and PPL electrolytes. This finding suggests that through the incorporation of Mod-SiO_2, PPLS-10 facilitates the formation of a dense and protective SEI layer with a high LiF content. Simultaneously, Mod-SiO_2 optimizes the chemical composition and structure of the SEI film by forming stable Si–O–C and Si–O–Li interfacial bonds (Fig. S12 in the ESM). This optimized SEI film effectively suppresses side reactions and reduces interfacial impedance, thereby enhancing the battery's cycling stability and rate performance. The results were further validated by analyzing the EIS of $LiFePO_4$/PPLS-10/Li, $LiFePO_4$/PPL/Li, and $LiFePO_4$/PL/Li batteries before and after cycling, along with SEM morphological analysis of the cycled lithium metal anodes. As shown in the figures (Fig. S13 in the ESM and Figs. 5(j)–5(l)), the PPLS-10 battery system exhibits lower internal resistance after cycling, while the lithium metal surface appears smoother and flatter. This indicates close interface contact and a stable interface environment between the solid-state electrolyte and the anode. The presence of uniform fillers effectively suppresses the formation and growth of lithium dendrites, thereby ensuring the battery's long-term stable cycling performance. Combined SEM and XPS analyses confirm that the PPLS-10 solid electrolyte, prepared by introducing Mod-SiO_2, effectively induces uniform lithium deposition.

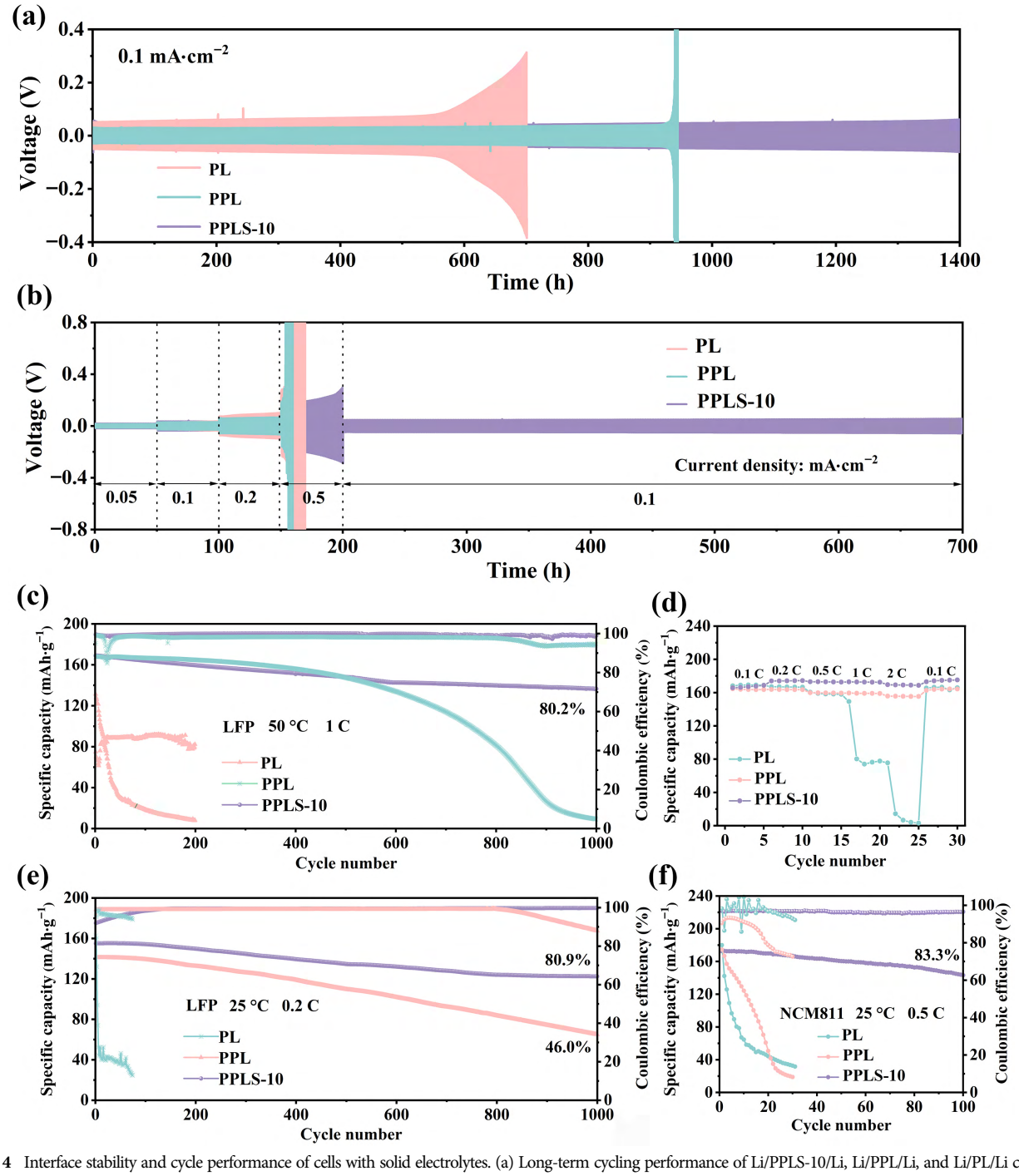

Figure 4 Interface stability and cycle performance of cells with solid electrolytes. (a) Long-term cycling performance of Li/PPLS-10/Li, Li/PPL/Li, and Li/PL/Li cells at a current density of 0.1 mA·cm^{-2}. (b) Rate performance tests of Li/PPLS-10/Li, Li/PPL/Li, and Li/PL/Li cells. (c) Long-term cycling performance of $LiFePO_4$/PPLS-10/Li, $LiFePO_4$/PPL/Li, and $LiFePO_4$/PL/Li cells at 50 °C and 1 C. (d) Rate capability comparison of $LiFePO_4$/PPLS-10/Li, $LiFePO_4$/PPL/Li, and $LiFePO_4$/PL/Li cells. (e) Long-term cycling performance of $LiFePO_4$/PPLS-10/Li, $LiFePO_4$/PPL/Li, and $LiFePO_4$/PL/Li cells at 25 °C and 0.2 C. (f) Cycling performance comparison of NCM811/PPLS-10/Li, NCM811/PPL/Li, and NCM811/PL/Li cells at 25 °C and 0.5 C.

Simultaneously, due to its excellent interfacial contact and minimal interfacial side reactions, it significantly enhances the cycling stability of lithium metal batteries.

To further investigate the interaction mechanism among Mod-SiO_2, the polymer matrix, and LiTFSI, a series of simulation calculations was performed. Molecular dynamics (MD) simulations were employed to analyze the diffusion kinetics of Li^+ within the PVDF-based electrolyte at the atomic level. As depicted in Figs. 6(a) and 6(b) and Figs. S14 and S15 in the ESM, the PPLS-10 electrolyte exhibits the highest lithium-ion diffusion coefficient across the tested temperature range. This result confirms that the incorporation of PAN enhances Li^+ transport capability. Furthermore, the addition of Mod-SiO_2 constructs a continuous ion-conductive network, which acts as a "highway" and significantly accelerates Li^+ transport. Notably, the active sites within this network also effectively impede the migration of $TFSI^-$ anions. According to the radial distribution function (RDF) analysis shown

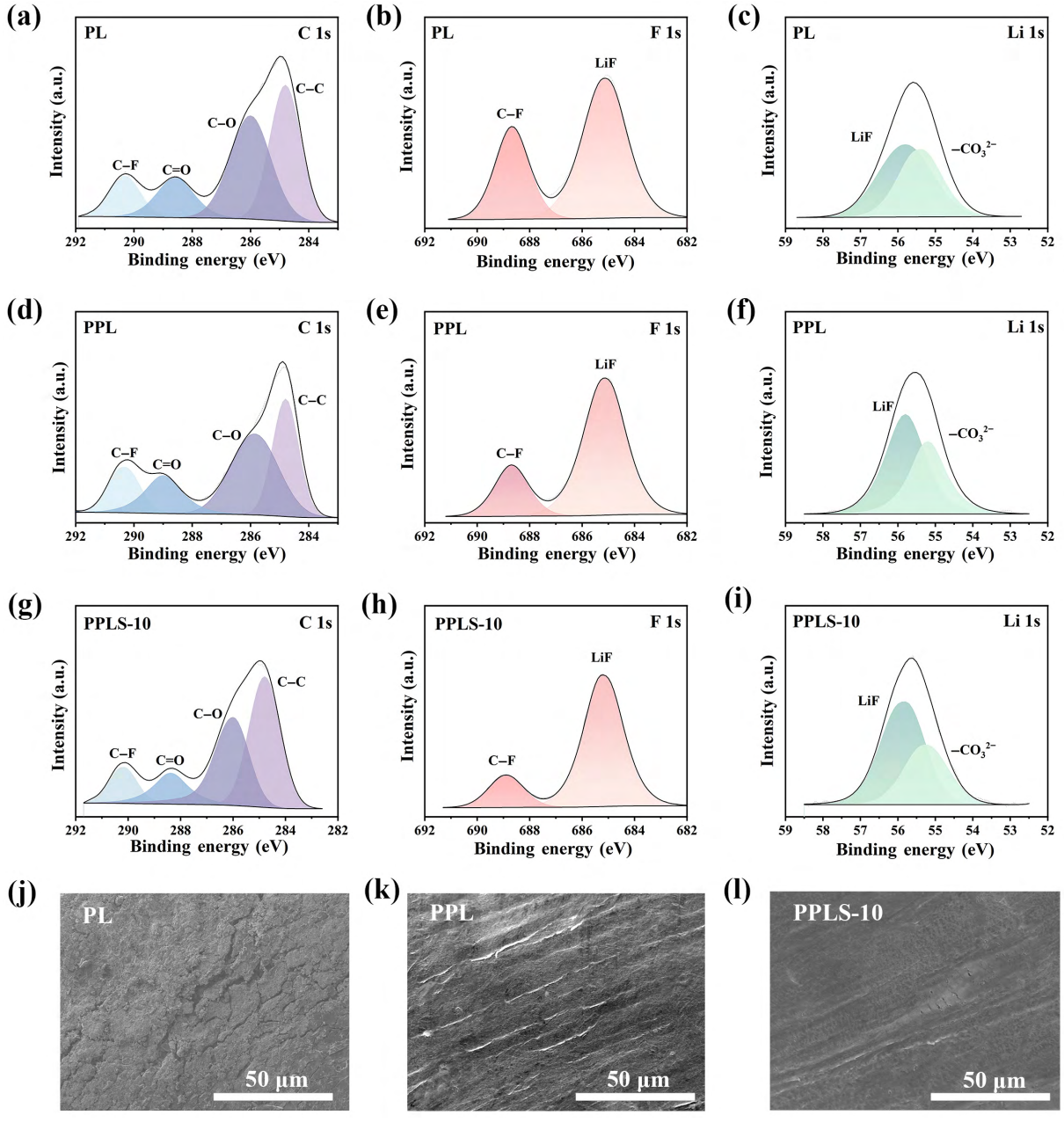

Figure 5 XPS spectra and top-view SEM images of cycled lithium metal anode surfaces in Li/PL/Li, Li/PPL/Li, and Li/PPLS-10/Li symmetric cells. (a) C 1s, (b) F 1s, and (c) Li 1s spectra for Li/PL/Li. Corresponding (d) C 1s, (e) F 1s, and (f) Li 1s spectra for Li/PPL/Li. Corresponding (g) C 1s, (h) F 1s, and (i) Li 1s spectra for Li/PPLS-10/Li. Top-view SEM images of cycled lithium metal anodes from the (j) $LiFePO_4$/PL/Li battery, (k) $LiFePO_4$/PPL/Li battery, and (l) $LiFePO_4$/PPLS-10/Li battery.

in Fig. 6(c), the interaction force between Li^+ and the nitrogen atoms of $TFSI^-$ is weakened in the PPLS-10 system compared to PL. This weaker binding allows Li^+ to be more freely dispersed within the electrolyte, thereby enhancing ion migration efficiency. In addition, the glass transition temperatures (T_g) of PL, PPL, and PPLS-10 were measured by differential scanning calorimetry (DSC) (Fig. S16 in the ESM). The T_g of PPLS-10 is as low as −53.29 °C, significantly lower than those of PPL and PL. This indicates that the synergistic effect of PAN and Mod-SiO_2 promotes the formation of amorphous regions within the electrolyte, providing more accessible pathways for Li^+ migration. To corroborate this finding, the specific volume of each electrolyte was calculated at various temperatures via MD simulations. The T_g values determined from the inflection points of the specific volume curves (Figs. 6(d)–6(f)) are in excellent agreement with the experimental DSC results. To quantitatively assess the interaction strength between components, three model systems were constructed: PVDF-$TFSI^-$, PVDF-PAN-$TFSI^-$, and PVDF-PAN-Mod-SiO_2-$TFSI^-$. Their binding energies were calculated and compared (Fig. 6(i)). The results reveal that the binding energy of $TFSI^-$ is highest in the system containing Mod-SiO_2, demonstrating that Mod-SiO_2 has a strong anchoring effect on the lithium salt anions. Based on these simulations, the introduction of Mod-SiO_2 serves a dual function: It promotes the dissociation of LiTFSI and simultaneously captures $TFSI^-$ anions. This process increases the concentration of free Li^+ while reducing the mobility and obstructive effect of $TFSI^-$, thereby synergistically enhancing the "highway effect" of the ion-conductive network and improving overall ionic conductivity (Figs. 6(g) and 6(h)).

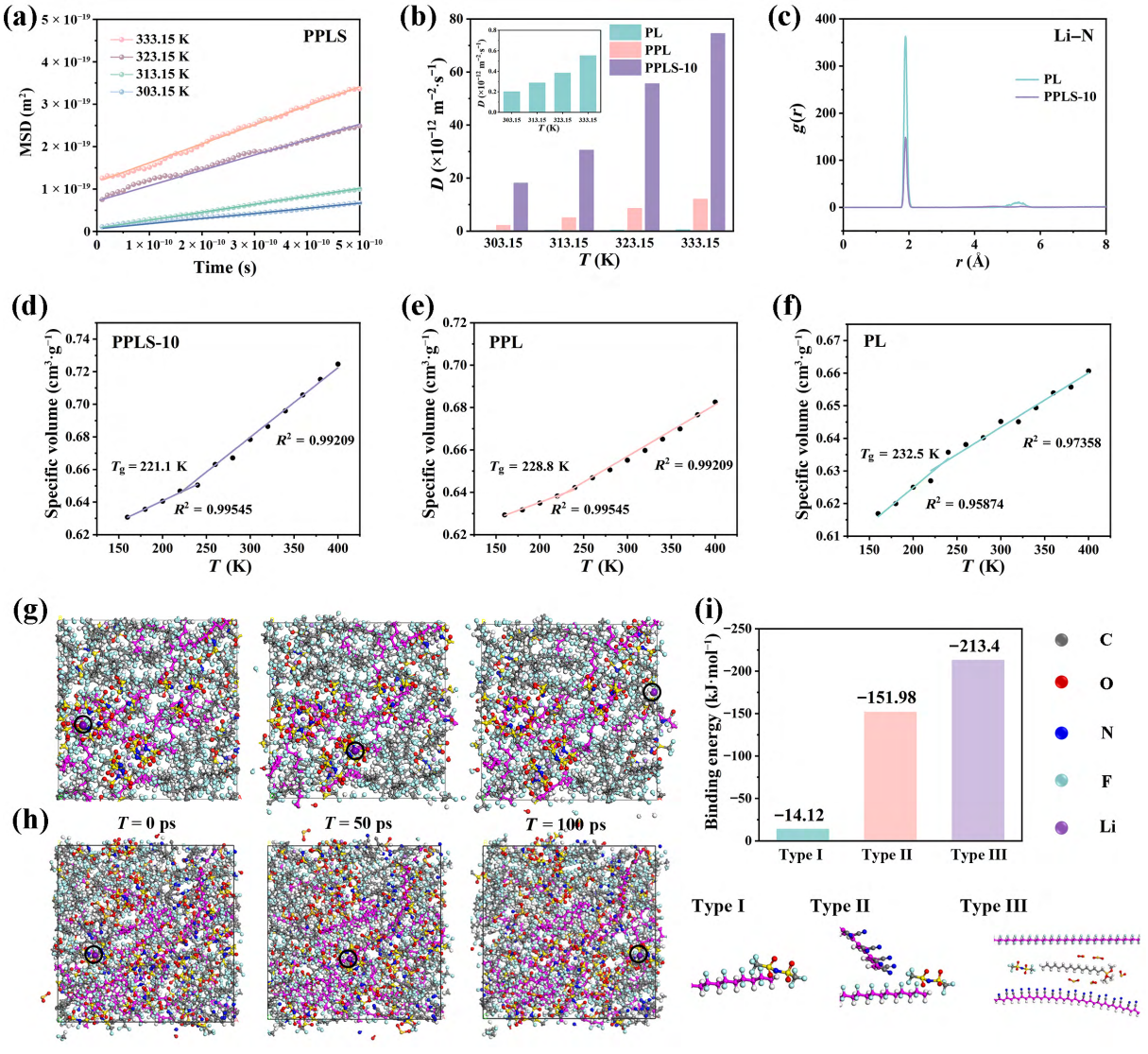

Figure 6 Theoretical calculations and MD simulations for solid electrolytes. (a) Mean square displacement (MSD) fitting curves of PPLS-10 at 313.15, 323.15, and 333.15 K. (b) Comparison of diffusion coefficients of PL, PPL, and PPLS-10 at different temperatures. (c) Comparison of the Li–N interaction forces between PL and PPLS-10 systems. (d)–(f) Fitting plots of T_g of PPLS-10, PPL, and PL from MD simulations. Simulation snapshots of (g) PL and (h) PPLS simulation boxes at 0, 50, and 100 ps, visualizing Li^+ transport processes. (i) Binding energy comparison among PVDF-$TFSI^-$ (Type I), PVDF-PAN-$TFSI^-$ (Type II), and PVDF-PAN-Mod-SiO_2-$TFSI^-$ (Type III) complexes.

3 Conclusions

In summary, an organic–inorganic synergistic modification strategy was successfully employed to fabricate a PVDF/PAN/Mod-SiO_2 composite solid-state electrolyte (PPLS-10). This electrolyte combines high ionic conductivity with outstanding interfacial stability, offering an innovative solution for solid-state lithium metal batteries. The long-chain alkyl structure of HDTMS effectively enhanced the compatibility between SiO_2 and the PVDF/PAN matrix. This modification significantly decreased the polarity of the NMP solvent, consequently mitigating the risk of side reactions between NMP and LiTFSI. Concurrently, the Lewis acid-base interaction between the Si–OH groups on the surface of SiO_2 and the $TFSI^-$ anions facilitated the dissociation of lithium salts. This interaction led to a synergistic enhancement among "dispersion–ionic conductivity–interfacial stability". The raw material cost used in this work is controllable and suitable for large-scale production. HDTMS solves the dispersion problem, adapts to various slurries, and facilitates the mass production of solid-state electrolytes. As a result, PPLS-10 exhibited an ionic conductivity of 4.83×10^{-4} S·cm^{-1} and a lithium-ion transference number of 0.7 at room temperature. The Li|PPLS-10|Li symmetric battery, based on this electrolyte, was capable of stable cycling for over 1400 h at a current density of 0.1 mA·cm^{-2}, thereby demonstrating exceptional compatibility with the lithium-metal interface. In the $LiFePO_4$ and NCM811 cathode systems, the respective half-cells maintained capacity retentions of 80.2% after 1000 cycles at a current rate of 1 C and 83.3% after 100 cycles at a current rate of 0.5 C. The organic–inorganic synergistic modification strategy proposed herein, through the integration of material design and interface engineering, presents a process-controllable electrolyte solution with excellent performance for the development of high-energy-density solid-state lithium-metal batteries. This strategy holds great promise for industrial applications.

Electronic Supplementary Material: Supplementary material (further details of the SEM image, EDS mapping, TGA chart, DSC scan, and battery performance test chart) is available in the online version of this article at https://doi.org/10.26599/NR.2026.94908656.

Data availability

All data needed to support the conclusions in the paper are presented in the manuscript and the Electronic Supplementary Material. Additional data related to this paper may be requested from the corresponding author upon request.

Acknowledgements

This research was supported by the National Natural Science Foundation of China (No. 52402257), 2025 Shaoyang City "Challenging the List and Taking Command" Science and Technology Project (No. 2025JB001), the Shandong Provincial Natural Science Foundation (No. ZR2024QE142), the China Postdoctoral Science Foundation under Grant (No. 2024M751105), Young Talent of Lifting Engineering for Science and Technology in Shandong China (No. SDAST2025QTA095), the Youth Innovation Team Project of Shandong Province (No. 2024KJH108), and University of Jinan Young Faculty Interdisciplinary Convergence Development Project 2025 (No. XKJC-202503). We thank the Analyzing & Testing Center from School of Chemistry and Pharmaceutical Engineering at the Changsha University of Science and Technology for characterizing of XPS and X-ray diffraction (XRD) data.

Declaration of competing interest

All the contributing authors report no conflict of interests in this work.

Author contribution statement

L. B. S.: Data curation, project administration, validation, funding acquisition. Y. Y. X.: Data curation, project administration, writing manuscript, experimental design. X. L. X.: Project administration, validation, funding acquisition. Z. L. X.: Project administration, funding acquisition, experimental design. T. Y. L.: Project administration, experimental design, writing manuscript. D. X. W.: Investigation, funding acquisition. Y. J. K.: Data curation, project administration. X. W.: Investigation, funding acquisition. T. T. Z.: Data curation, project administration, writing – review & editing. F. L. C.: Writing – review & editing, methodology, funding acquisition. All the authors have approved the final manuscript.

Use of AI statement

None.

References

[1] Zhang, H. L.; Zhao, H. B.; Khan, M. A.; Zou, W. W.; Xu, J. Q.; Zhang, L.; Zhang, J. J. Recent progress in advanced electrode materials, separators and electrolytes for lithium batteries. *J. Mater. Chem. A* **2018**, *6*, 20564–20620.

[2] Zhou, D.; Shanmukaraj, D.; Tkacheva, A.; Armand, M.; Wang, G. X. Polymer electrolytes for lithium-based batteries: Advances and prospects. *Chem* **2019**, *5*, 2326–2352.

[3] Sun, S. Y.; Wang, K. H.; Hong, Z. L.; Zhi, M. J.; Zhang, K.; Xu, J. J. Electrolyte design for low-temperature Li-metal batteries: Challenges and prospects. *Nano-Micro Lett.* **2024**, *16*, 35.

[4] Sen, S.; Trevisanello, E.; Niemöller, E.; Shi, B. X.; Simon, F. J.; Richter, F. H. The role of polymers in lithium solid-state batteries with inorganic solid electrolytes. *J. Mater. Chem. A* **2021**, *9*, 18701–18732.

[5] Dirican, M.; Yan, C. Y.; Zhu, P.; Zhang, X. W. Composite solid electrolytes for all-solid-state lithium batteries. *Mat. Sci. Eng. R: Rep.* **2019**, *136*, 27–46.

[6] Ke, X. Y.; Wang, Y.; Dai, L. M.; Zhang, X. W. Cell failures of all-solid-state lithium metal batteries with inorganic solid electrolytes: Lithium dendrites. *Energy Storage Mater.* **2020**, *33*, 309–328.

[7] Chen, X. Y.; Gao, X. J.; Wu, H. Y.; Liu, Y. L.; Yang, X. F.; Sun, R. C. Lignin-reinforced PVDF electrolyte for dendrite-free quasi-solid-state Li metal battery. *Rare Met.* **2024**, *43*, 1006–1016.

[8] Song, L. B.; Xiong, Y. Y.; Xiao, Z. L.; Li, A.; Yan, L. X.; Kuang, Y. J.; Zhao, T. T. Research progress on the mechanism and key role of filler structure on properties of PVDF composite solid electrolyte. *Ionics* **2024**, *30*, 5861–5877.

[9] Zhou, S. Y.; Zhong, S. J.; Dong, Y. F.; Liu, Z. Z.; Dong, L. W.; Yuan, B. T.; Xie, H. D.; Liu, Y. P.; Qiao, L.; Han, J. C. et al. Composition and structure design of poly(vinylidene fluoride)-based solid polymer electrolytes for lithium batteries. *Adv. Funct. Mater.* **2023**, *33*, 2214432.

[10] Lin, X. D.; Zhou, G. D.; Liu, J. P.; Yu, J.; Effat, M. B.; Wu, J. X.; Ciucci, F. Rechargeable battery electrolytes capable of operating over wide temperature windows and delivering high safety. *Adv. Energy Mater.* **2020**, *10*, 2001235.

[11] Cheng, X.; Bae, J. DNA: Novel crystallization regulator for solid polymer electrolytes in high-performance lithium-ion batteries. *Nanomaterials* **2024**, *14*, 1670.

[12] Sun, Q. F.; Bi, Z. J.; Chen, X.; Wang, N.; Zhong, G. M.; Peng, Z. Q.; Lin, J.; Guo, X. X. Revealing critical roles of alkaline passivation layer on garnet surface toward poly(vinylidene fluoride)-based composite electrolytes for solid-state lithium batteries. *J. Colloid Interf. Sci.* **2025**, *683*, 678–687.

[13] Ma, Y. T.; Chen, L. K.; Li, Y. H.; Li, B. Y.; An, X. F.; Cheng, X.; Su, H.; Yang, K.; Xiao, G. Y.; Zhao, Y. et al. Mesoscale polymer regulation for fast-charging solid-state lithium metal batteries. *Energy Environ. Sci.* **2025**, *18*, 3730–3739.

[14] Hou, H. Y.; Huang, B. X.; Yu, X. H.; Lan, J.; Ming, S.; Rong, J.; Liu, X. X.; Chen, F. S. Compatible composite electrolyte membrane $Li_7La_3Zr_2O_{12}$/SB-PVDF for solid-state lithium ion battery. *J. Energy Storage* **2023**, *68*, 107680.

[15] Wang, W. J.; Jia, M. Y.; Bi, Z. J.; Guo, X. X. Porous g-C_3N_4 microspheres wrapped by garnet nanoparticles enable solid composite electrolytes with improved ionic conduction and interfacial stability. *Adv. Funct. Mater.* **2025**, *35*, 2419182.

[16] Liu, J. G.; Li, B. H.; Cao, J. H.; Xing, X.; Cui, G. Challenges in Li-ion battery high-voltage technology and recent advances in high-voltage electrolytes. *J. Energy Chem.* **2024**, *91*, 73–98.

[17] Thomas, F.; Mahdi, L.; Lemaire, J.; Santos, D. M. F. Technological advances and market developments of solid-state batteries: A review. *Materials* **2024**, *17*, 239.

[18] Xie, W. H.; Deng, Z. Y.; Liu, Z. Y.; Famprikis, T.; Butler, K. T.; Canepa, P. Effects of grain boundaries and surfaces on electronic and mechanical properties of solid electrolytes. *Adv. Energy Mater.* **2024**, *14*, 2304230.

[19] Lu, T. L.; Meng, S.; Liu, M. Electrochemically and chemically stable electrolyte–electrode interfaces for lithium iron phosphate all-solid-state batteries with sulfide electrolytes. *J. Mater. Chem. A* **2024**, *12*, 3954–3966.

[20] Pei, F.; Wu, L.; Zhang, Y.; Liao, Y. Q.; Kang, Q.; Han, Y.; Zhang, H. W.; Shen, Y.; Xu, H. H.; Li, Z. Interfacial self-healing polymer

electrolytes for long-cycle solid-state lithium–sulfur batteries. *Nat. Commun.* **2024**, *15*, 351.

[21] Zhu, J. X.; Li, X. L.; Wu, C. W.; Gao, J.; Xu, H. H.; Li, Y. T.; Guo, X. X.; Li, H.; Zhou, W. D. A multilayer ceramic electrolyte for all-solid-state Li batteries. *Angew. Chem., Int. Ed.* **2021**, *60*, 3781–3790.

[22] Liu, J.; Pei, L.; Li, J. L. Three-dimensional continuous ion transport skeleton-reinforced composite solid electrolyte for high-performance solid-state lithium metal batteries. *ACS Appl. Mater. Interfaces* **2025**, *17*, 33002–33014.

[23] Liu, X. Z.; Wang, D.; Wang, X. T.; Wang, D. Y.; Li, Y.; Fu, J.; Zhang, R.; Liu, Z. Y.; Zhou, Y. Z.; Wen, G. W. Designing compatible ceramic/polymer composite solid-state electrolyte for stable silicon nanosheet anodes. *Small* **2024**, *20*, 2309724.

[24] Zhai, P. B.; Yang, Z. L.; Wei, Y.; Guo, X. X.; Gong, Y. J. Two-dimensional fluorinated graphene reinforced solid polymer electrolytes for high-performance solid-state lithium batteries. *Adv. Energy Mater.* **2022**, *12*, 2200967.

[25] Jiang, H.; Du, Y. Q.; Liu, X. Y.; Kong, J. R.; Huang, M. Q.; Liu, P.; Zhou, T. Composite polymer electrolytes incorporating two-dimensional metal–organic frameworks for ultralong cycling in solid-state lithium batteries. *J. Mater. Chem. A* **2023**, *11*, 22371–22383.

[26] Yu, X. J.; Zhai, P. B.; Zhao, N.; Guo, X. X. *In-situ* plasticized LLZTO-PVDF composite electrolytes for high-performance solid-state lithium metal batteries. *Batteries* **2023**, *9*, 257.

[27] Zhang, Z. H.; Fan, R. Z.; Huang, S. F.; Zhao, J.; Zhang, Y. D.; Dai, W. J.; Zhao, C. J.; Song, X.; Cao, P. Integrated design of a functional composite electrolyte and cathode for all-solid-state Li metal batteries. *Batteries* **2023**, *9*, 320.

[28] Yuan, Y.; Wang, B.; Xue, K. S.; Ma, Y. T.; Liu, X. Y.; Peng, X. P.; Liu, M. B.; Lu, H. High-voltage solid-state lithium metal batteries with stable anodic and cathodic interfaces by a laminated solid polymer electrolyte. *ACS Appl. Mater. Interfaces* **2023**, *15*, 17144–17151.

[29] Tran, H. K.; Truong, B. T.; Zhang, B. R.; Jose, R.; Chang, J. K.; Yang, C. C. Sandwich-structured composite polymer electrolyte based on PVDF-HFP/PPC/Al-doped LLZO for high-voltage solid-state lithium batteries. *ACS Appl. Energy Mater.* **2023**, *6*, 1475–1487.

[30] Wang, W. Q.; Xia, C.; Zhu, C. T.; Wu, Y. Y.; Cao, J. H.; Li, Y.; Wu, D. Y. Effects of LATP particle size on the residual moisture of separator coating and the performance of NCM811 batteries. *ACS Appl. Mater. Interfaces* **2025**, *17*, 22727–22737.

[31] Wu, J.; Shi, L. R.; Li, J.; Xu, J. C.; Feng, T.; Guo, W. Design and study of semi-solid-state lithium-ion battery based on LATP electrolyte. *J. Energy Storage* **2025**, *120*, 116487.

[32] Yi, X. R.; Guo, Y.; Chi, S. J.; Pan, S. Y.; Geng, C. N.; Li, M. Y.; Li, Z. S.; Lv, W.; Wu, S. C.; Yang, Q. H. Surface Li_2CO_3 mediated phosphorization enables compatible interfaces of composite polymer electrolyte for solid-state lithium batteries. *Adv. Funct. Mater.* **2023**, *33*, 2303574.

[33] Wang, S. J.; He, L.; Wang, M. T.; Guo, X. T.; Chen, R. T.; Qiu, X. Y.; Kudashev, S.; Wei, T.; Wang, Q. The applications of IL@MOFs for solid-state electrolytes in all-solid-state battery: A review. *J. Mater. Sci.* **2024**, *59*, 8650–8668.

[34] Song, L. B.; Long, T. Y.; Xiao, M. Z.; Liu, M.; Zhao, T. T.; Kuang, Y. J.; Jiang, L.; Xiao, Z. L. Improvement of ionic conductivity of solid polymer electrolyte based on Cu–Al bimetallic metal–organic framework fabricated through molecular grafting. *Trans. Nonferr. Metals Soc. China* **2024**, *34*, 2943–2958.

[35] Ma, Y. T.; Qiu, Y.; Yang, K.; Lv, S.; Li, Y. H.; An, X. F.; Xiao, G. Y.; Han, Z.; Ma, Y. T.; Chen, L. K. et al. Competitive Li-ion coordination for constructing a three-dimensional transport network to achieve ultra-high ionic conductivity of a composite solid-state electrolyte. *Energy Environ. Sci.* **2024**, *17*, 8274–8283.

[36] Liu, Y. X.; Wang, S. Q.; Chen, W. C.; Kong, W. H.; Wang, S. P.; Liu, H. X.; Ding, L.; Ding, L. X.; Wang, H. H. 5.1 μm ion-regulated rigid quasi-solid electrolyte constructed by bridging fast Li-ion transfer channels for lithium metal batteries. *Adv. Mater.* **2024**, *36*, 2401837.

[37] Wang, C.; Li, W. X.; Li, D. B.; Zhao, X. X.; Li, Y.; Zhang, Y. L.; Qi, X.; Wu, M.; Fan, L. Z. High-performance solid-state lithium metal batteries of garnet/polymer composite thin-film electrolyte with domain-limited ion transport pathways. *ACS Nano* **2024**, *18*, 32175–32185.

[38] Li, X.; Pan, H. W.; Yin, G. J.; Xiang, Y.; Lin, X. T.; Liu, Z.; Jiang, Y. Z.; Hui, Q.; Zhang, X.; Xu, M. W. Achieving multifunctional MOF/polymer-based quasi-solid electrolytes via functional molecule encapsulation in MOFs. *Inorg. Chem. Front.* **2025**, *12*, 4438–4448.

[39] Li, M. L.; An, H. W.; Song, Y. J.; Liu, Q. S.; Wang, J.; Huo, H.; Lou, S. F.; Wang, J. J. Ion-dipole-interaction-induced encapsulation of free residual solvent for long-cycle solid-state lithium metal batteries. *J. Am. Chem. Soc.* **2023**, *145*, 25632–25642.

[40] Ma, Y. T.; Wang, C. R.; Yang, K.; Li, B. Y.; Li, Y. H.; Guo, S. K.; Lv, J. S.; An, X. F.; Liu, M.; He, Y. B. et al. Ultrathin and robust composite electrolyte for stable solid-state lithium metal batteries. *ACS Appl. Mater. Interfaces* **2023**, *15*, 17978–17985.